Experimental Mechanics (2007) 47: 133–142
DOI 10.1007/s11340-006-8884-0

Nanoindentation and Microindentation of CuAlNi Shape Memory Alloy

W.C. Crone · H. Brock · A. Creuziger

Received: 15 November 2005 / Accepted: 18 April 2006 / Published online: 13 July 2006

Abstract Nanoindentation and microindentation studies were conducted within individual grains of a CuAlNi shape memory alloy. Linear surface features were observed near the indentations after unloading, many of which were responsive to heating. Crystallographic orientation information was obtained from electron backscattering diffraction in order to compare the orientation of observed surface features to predicted austenite–martensite interfaces, slip planes, and possible fracture planes in this alloy. Most of the features observed can be attributed to austenite–martensite interfaces, which remain in the material after unloading due to the constraints of the plastic deformation created by indentation. Due to the temperature dependence of the transformation stress in shape memory alloys, these stress-induced martensites are observed to diminish with heating and to reappear with cooling. Plastic deformation is observed in the form of pile-up near the indentation.

W.C. Crone (✉, SEM member)
Department of Engineering Physics,
University of Wisconsin—Madison,
1500 Engineering Drive,
Madison, WI 53706, USA
e-mail: crone@engr.wisc.edu

H. Brock
Materials Science Program,
University of Wisconsin—Madison,
1509 University Ave.,
Madison, WI 53706, USA

A. Creuziger (SEM member)
Engineering Mechanics Program,
University of WIsconsin—Madison,
1500 Engineering Drive,
Madison, WI 53706, USA

Keywords Nanoindentation · Microindentation · AFM · Shape memory alloy · CuAlNi

Introduction

Instrumented nanoindentation is an important tool for characterization of material properties at small scales. It has been widely used as a quantitative technique for determination of properties such as hardness and elastic modulus since the early 1990s [1]. More recently, nanoindentation is being used to investigate shape memory alloys (SMAs) such as NiTi [2–5] and CuAlNi [6–8], which are materials capable of undergoing a reversible solid-state phase transformation. The results of such testing in SMAs are much more difficult to interpret due to the added complexity of a phase transformation that can be induced by stress or temperature. These transformations occur between the high-symmetry austenite phase and the low-symmetry martensite phase for these materials.

Our work focuses on nano- and microindentation within large single grains of CuAlNi. A limited amount of prior work has been conducted on CuAlNi in an attempt to assess hardness [6], elastic modulus [6] and recovery ratio with heating [7, 8]. As in NiTi [3, 9], significant recovery of an indentation is reported when a sample is heated past transformation [6–8]. The hardness and modulus values reported are questionable because of stress induced transformation and martensite variant rearrangement that may occur during indentation.

Phenomenological models have been proposed for the processes occurring under an indenter in SMAs [3, 10, 11]. It is suggested that there is interplay between elastic deformation, plastic deformation, phase transformation and variant rearrangement. When indenting the austenite phase, it is expected that the material beneath the indenter undergoes elastic deformation of the austenite phase followed by stress-induced martensite transformation, martensite variant rearrangement, elastic deformation of the martensite phase, and finally plastic deformation. The process zone under the indenter is expected to contain material volumes in each of these states. Upon release of the indenter, some degree of recovery of elastic deformation and reversal of transformation are expected.

When indenting the martensite phase, elastic deformation of martensite is expected, along with martensite rearrangement and finally plastic deformation. With release of the indenter, elastic recovery and some martensite rearrangement may occur. Further recovery of the indent can be achieved through transformation of the martensite to austenite by heating above the transition temperature.

Direct evidence supporting all of these processes taking place under the indenter is limited, although the occurrence of transformation can be deduced from the behavior observed. From prior work it is hypothesized that micro or nanoindentation of NiTi produces stress-induced martensitic transformation followed by reorientation of the martensitic variants with additional loading [2, 4, 5, 10, 11] and inelastic deformation through dislocations [5, 10, 11]. Some surface deformation has been observed near indents in single crystal NiTi [10], but none in CuAlNi. Post indentation, it is possible to use the shape memory effect in NiTi to produce partial recovery of the deformation with heating [3, 9]. Similarly in CuAlNi, measurable recovery of nanoindentation depth and width with heating has been observed [6–8].

Using carefully prepared CuAlNi samples, deformations produced by nano- and microindentations in CuAlNi are investigated and the origin of surface features produced near the indentations and their response to heating are explored.

Theoretical Background

By using energy minimizing deformations and deformation sequences, all of the possible austenite–martensite transformations can be predicted from the unit cell structure of the austenite and martensite. Some of the possible microstructures and restrictions on the unit cells are given in [12]. Specific examples of the cubic to trigonal [13], cubic to orthorhombic [14], and cubic to monoclinic-I [15] transformations are in separate articles. The cubic to monoclinic-II is available in [16, 17]. Most of these topics are included in [16]. The review article [18] is a good summary of this work. CuAlNi deforms by monoclinic-II deformation, though the monoclinic angle is small enough that this structure approximated as orthorhombic with good agreement [19].

For a general microstructure interface the compatibility equation is $\mathbf{F}^{(i)} - \mathbf{U}^{(j)} = \mathbf{a} \otimes \mathbf{n}$, where **F** is the deformation gradient tensor, **U** is the transformation stretch, **a** is the amplitude of the deformation gradient jump, **n** is the normal of the interface surface and i and j are variants. This equation is known as the Hadamard compatibility condition. From the transformation stretches, a compatibility relation for an austenite–martensite interface can be developed. For an austenite–single variant of martensite interface, this compatibility is reached if:

$$\mathbf{R}\mathbf{U}^{(i)} - \mathbf{I} = \mathbf{b} \otimes \mathbf{m}, \tag{1}$$

where **R** is a rotation matrix for the martensite variant, **b** is the ‘shape strain’ and **m** is the ‘habit plane normal,’ which is the unit vector normal to the plane between the austenite and martensite phases. This relation restricts the eigenvalues in $\mathbf{U}(i)$ to have one value equal to one, one value less than one and one value greater than one. In general this condition is only met in a few special cases. Twinned martensite is a less restrictive solution to create an austenite–martensite interface. The compatibility condition for an austenite–twinned martensite interface is:

$$\mathbf{R}'\left(\lambda\mathbf{R}\mathbf{U}^{(i)} + (1-\lambda)\mathbf{U}^{(j)}\right) - I = \mathbf{b} \otimes \mathbf{m} \tag{2}$$

for $i \neq j$, where $\mathbf{R}'$ is the habit plane rotation and λ is the volume fraction of variant i. While still restrictive, many materials display this type of interface, including CuAlNi. The discussion below will refer to this type of interface as an austenite–martensite interface.

Experimental Techniques

A CuAlNi (13.9 at.% Al, 3.9 at.% Ni, balance Cu) sample measuring 5.75 mm by 5.75 mm by 1.5 mm was cut using electrical discharge machining from a boule prepared by Special Metals Inc. The sample was heat treated in argon at 900°C for 60 min and quenched in ice water. This heat treatment produces an austenite finish temperature of ~0°C (observed optically). All testing was conducted at room temperature, in the austenite phase.

In preparation for nanoindentation using atomic force microscopy (AFM), the CuAlNi sample was electropolished to provide a deformation-free surface. This preparation facilitated electron backscatter diffraction (EBSD) to determine the crystallographic orientation and provided surface conditions in which the effects of nanoindentation were evident. EBSD analysis was performed using a LEO 1530 scanning electron microscope (SEM). For electropolishing, a 50 vol.% solution of phosphoric acid in a 250 ml stainless steel beaker on a VWR 575 Digital Hotplate Stirrer was used. Three separate electropolishing treatments were preformed in sequence: 15 min with a 2 V potential with a stirring speed of 250, 10 min at 1 V stirring at a speed of 250, 10 min at 1 V stirring at a speed of 150. Despite the scattered pitting that occurred, there was adequate area in which to make indents. These pits are visible in the optical and AFM figures as circular depressions. (Work continues toward finding a more satisfactory electropolishing treatment for large samples).

A NanoScope IV atomic-force microscope stage with “J” type scanner was used for the indentations and subsequent imaging. Information about the force applied, distance traveled, and drift velocity is available from a Hysitron Transducer connected to Digital Instruments Inc. Nanoscope software version 5.12b51. This software provides a user interface to control the movement and position of the scanning tips, verify proper engagement with the surface, and for image capture. To control vibration the Hysitron stage was placed atop a Minus K BM-4 Bench Top Vibration Isolation Platform, which is capable of damping frequencies down to 0.5 Hz in the vertical and horizontal directions. While this platform damps out vibrations quickly, a wait time of at least 15 min was observed as a precaution prior to indenting to allow the electronics to equilibrate.

After calibration of the electronics, the indenter tip is slowly lowered to the surface using Hysitron Inc. Triboscope software version 3.6.0.1, a user interface for controlling the indentation process and gathering indentation data. Once contact is made and deemed stable, preliminary scans of the area are done and indents made in appropriate locations. The indents, created under an applied force of 9,000 μN using a diamond Berkovich tip, are triangular in shape with a triangular altitude of less than 2 μm and a depth between 400 and 700 nm. The tip radius of the Berkovich indenter is nominally 150–200 nm and the angle of the obtuse tip is 142°. A force-displacement plot was obtained for each indent. The sample was aligned to correlate with crystallography information obtained from EBSD. It is apparent from AFM images that the Berkovich tip itself remains in the same orientation as well.

Prior to indentation, landmarks were located on the sample surface and a large preliminary contact mode AFM scan was made. The Berkovich tip, used for both indentation and initial imaging, was positioned over the target area and another similarly large scan carried out. Prior to each indentation the scan size was gradually decreased to diminish tip drift once a suitable location for indentation was chosen.

Following indentation a scan was made with a contact mode silicon nitride AFM tip. The purpose of the contact mode scan is to image the surface with better resolution than can be achieved with the indenter tip. Two sets of data were acquired from these scans: relative height and tip deflection. The latter is primarily useful for visualizing surface morphology, while the height data provides a better quantitative description of topography.

In addition to nanoindentation, microindentation was conducted using a Buehler MicroMet2003 and a Vickers indenting tip, applying forces between 0.5 and 1.0 N. The microindentations were also made at two different angles to examine the indenter orientation dependence of the deformation. The microindentations were observed using a Nikon Eclipse optical microscope equipped with differential interference contrast (DIC), which employs a Nomarski prism in the light path to create a false color representation of surface tilt. In all cases the reference edge used in EBSD was also used during optical imaging.

There is a difference of 3° between the AFM image reference edge and the reference edge of the images taken under the optical microscope. All results are given in the frame of the AFM images, thus the observed angles reported in Tables 1 and 2 for the microindentations have been rotated 3° clockwise. The reference edge is dictated by the EBSD output, and all angles are measured counter clockwise from the left edge for all images.

Experimental Results

For the purposes of this research, two grains (identified as Grain A and Grain B) were studied in detail. Representative load–displacement curves obtained during nanoindentation are presented in Fig. 1. The time to maximum load was 80 s with a hold at 9,000 μN for 10 s followed by another 80 s to withdraw to the initial indenter position. The inset in Fig. 1 shows an inverse pole figure obtained from EBSD identifying the crystallographic orientation of each grain. Although these two grains are substantially different in orientation, the mechanical response under indentation is nearly identical.

Using the procedure described above, a number of parallel linear features were observed near the site of indentation in both nanoindentations and microindentations. In some cases, parallel linear features appear on both sides of the indent. Figure 2, obtained from AFM deflection data, shows these features surrounding a representative nanoindentation. The angles of these indentation-induced features with respect to the reference frame described above are −88.5°, −42°, −22° and +76° for Grain A (see Observed Angles in Table 1) and −30.5° and 29° for Grain B (see Observed Angles Table 2). Experimental error is estimated to be ±3° for nanoindentation measurements.

Table 1 Experimentally observed angles of linear features and analytical results for the intersection of the austenite–martensite (A–M) interfaces, slip planes, and fracture planes with the crystallographic plane of observation for Grain A

Grain A				
Observed angles			**Nano** **−88.5** ± **3** **−42** ± **3** **−22** ± **3** **76** ± **3**	*Micro* *−62* ± *2* *−17* ± *2* *65* ± *2*
A-M Interfaces			Slip Planes	Fracture Planes
−86.9	−29.6	29.6	110 planes	566 planes
−84.9	−29.0	30.1	−*61.7*	−72.3
−84.7	−28.4	30.6	−*61.7*	−64.1
−80.7	−28.2	30.6	**−23.9**	−*64.0*
−80.5	**−20.8**	31.7	**−23.9**	−*60.1*
−80.1	**−19.8**	31.9	1.2	−57.6
−77.5	−*15.3*	34.4	1.2	−55.5
−76.8	−*15.1*	34.4	29.3	11.4
−67.6	−14.2	36.9	29.3	18.8
−67.2	−13.8	36.9	53.7	20.3
−65.8	−12.0	37.4	53.7	39.0
−65.8	−10.8	37.6	85.2	40.4
−65.0	−7.1	38.1	85.2	48.5
−64.7	−6.9	40.0		
−*63.8*	−6.6	42.8	111 planes	765 planes
−*63.6*	−6.3	44.5	−64.6	−77.4
−59.4	12.3	*65.8*	−59.9	−73.5
−59.3	14.3	*66.8*	16.8	−69.4
−58.7	17.1	67.2	42.6	−67.9
−58.3	20.1	68.2		−64.2
−58.1	20.7	68.2	211 planes	−*63.7*
−57.1	20.9	68.2	**−85.8**	−58.1
−57.0	21.4	70.2	−77.3	−57.9
−56.5	21.9	71.4	−70.3	−56.3
−41.7	23.5	**73.6**	−58.7	−55.3
−41.0	24.2	**73.6**	**−43.6**	−51.9
−39.0	26.4	**75.1**	**−40.4**	−51.5
−38.8	27.0	**76.5**	4.6	8.8
−37.6	27.9	**78.9**	6.1	9.4
−34.4	28.0	**79.0**	19.8	15.7
−33.8	28.5	79.7	38.3	18.2
−32.1	29.1	80.2	54.8	23.6
			55.4	25.4
				33.5
				35.4
				41.4
				43.6
				50.7
				51.0

Table 2 Experimentally observed angles of linear features and analytical results for the intersection of the austenite–martensite (A–M) interfaces, slip planes, and fracture planes with the crystallographic plane of observation for Grain B

Grain B				
Observed angles			**Nano** **−30.5** ± **3** **29** ± **3**	*Micro* *−67.5* ± *2* *−38* ± *2* *−22* ± *2* *10* ± *2* *36.5* ± *2* *80.5* ± *2*
A-M Interfaces			Slip Planes	Fracture Planes
−84.6	−*21.2*	**30.8**	110 planes	566 planes
−83.5	−19.6	**30.9**	−*67.0*	−79.4
−81.6	−19.0	**31.9**	−*67.0*	−74.0
−79.7	−16.2	**32.0**	**−28.4**	−65.1
−79.1	−14.6	*35.4*	**−28.4**	−62.0
−78.0	−14.5	*35.9*	**26.3**	−57.0
−76.9	−12.9	*36.1*	**26.3**	2.2
−76.3	−12.5	*36.2*	**28.9**	*8.9*
−75.9	−12.2	*36.9*	**28.9**	*10.3*
−75.1	−10.3	*38.5*	33.1	49.9
−75.1	−0.4	*38.5*	33.1	52.5
−72.4	0.1	39.5	89.8	59.3
−70.0	2.0	40.2	89.8	*81.4*
−*68.3*	*11.5*	40.2		
−*68.3*	*11.5*	40.6	111 planes	765 planes
−*67.1*	12.6	41.6	−84.3	88.7
−*66.8*	13.0	41.8	−61.4	−88.1
−65.4	16.8	44.9	7.1	−83.7
−65.1	16.9	46.4	53.9	−81.8
−63.0	17.8	48.3		**−30.7**
−62.6	18.6	50.0	211 planes	**−29.6**
−61.5	19.2	50.3	−79.6	−26.4
−60.2	20.3	52.0	−58.6	−25.2
−59.8	21.9	52.3	−45.7	−19.4
−44.1	22.1	73.7	−40.2	−18.7
−43.5	22.9	74.4	−7.8	−17.4
−41.6	23.2	77.2	0.4	−14.2
−41.3	23.8	77.2	15.8	−14.1
−40.5	24.3	77.7	**27.9**	−1.4
−*37.2*	24.9	*80.9*	**30.0**	15.1
−*37.1*	**26.0**	*82.2*	58.5	18.9
−35.3	**26.0**	83.7	74.4	34.4
			76.8	*37.4*
				40.7
				45.7
				50.2
				52.0
				82.5
				83.7

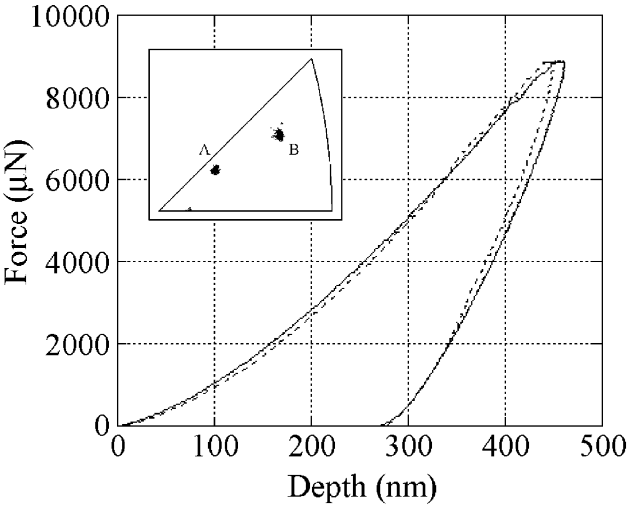

$$\overset{\underline{\text{Grain A}}}{\begin{bmatrix} .918 & .292 & .269 \\ -.347 & .919 & .185 \\ -.193 & -.263 & .945 \end{bmatrix}} \quad \overset{\underline{\text{Grain B}}}{\begin{bmatrix} .839 & .227 & .495 \\ -.436 & .824 & .361 \\ -.326 & -.519 & .790 \end{bmatrix}}$$

Fig. 1. Load-displacement curves from nanoindentation conducted in Grain A and Grain B. The *dotted line* corresponds to Grain A and the *solid line* corresponds to Grain B. The inset inverse pole figure (*IPF*) from EBSD shows the orientation of the grains. The matrices produced by EBSD for Grains A and B provide the rotation from the crystallographic axes to the

Figure 3 provides detailed AFM data for Grain A and Grain B. Section data is taken along a line perpendicular to the linear features near one side of the indentation. The length of these linear features is up to 2 μm while the relative height from the surface is up to 11 nm, for an indent depth of up to 660 nm.

Subsequent to nanoindentation studies, microindentations were created in the two grains and studied optically. Figure 4 shows two similarly oriented indentations within the two neighboring Grains A and B, while Fig. 5 shows two indents of different orientation in Grain B. In both nanoindentations and microindentations, the orientation of the linear features observed varies from grain to grain, and the number of lines varies to some degree from indent to indent. There is also evidence that these features depend on the geometry and orientation of the indenter from differences observed between the Berkovich nanoindentations and the Vickers microindentations as well as difference observed when the microindenter was rotated with respect to the crystal. The angles of these indentation-induced features with respect to the reference frame described above are −62°, −17°, +65° for Grain A (see Observed Angles in Table 1) and −67.5°, −38°, −22°, +10°, +36.5°, and +80.5° for Grain B (see Observed Angles Table 2). Not all angles are observed surrounding each indentation, although with only one exception every angle was observed surrounding at least two differently oriented indentations. Experimental error is estimated to be ±2° for microindentation measurements.

Following the initial optical observations of the microindentations, thermal experiments were conducted on a heating stage in the optical microscope. Optical DIC images were taken at room temperature and after heating to 90°C. As the images in Fig. 6 demonstrate, some of the surface features observed after microindentation diminish or vanish as a consequence of heating. Among the various microindentations studied, features at every angle except +65° were observed to diminish or vanish in at least one case of their occurrence.

Analytical Results

Using the compatibility condition described by equation 2 above, the **b** and **m** vectors can be calculated for an austenite–twinned martensite interface [20, 21], given lattice parameters alpha = 1.04245, beta = 0.9178, and delta = 0.01945. It is then possible to rotate these vectors from the crystallographic coordinate system into the sample coordinate system and compare these predicted austenite–martensite interfaces to the observed structures.

In addition to austenite–martensite type structures, slip and fracture may also be observed in CuAlNi. For thoroughness, the planes these occur on are also considered potential explanations for the linear fea-

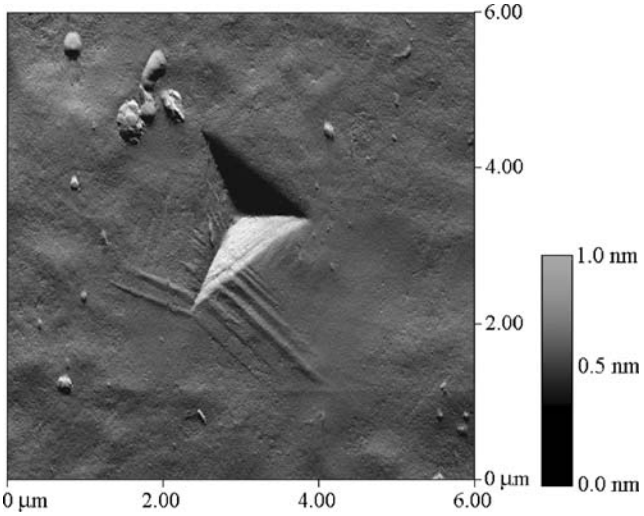

Fig. 2. AFM image of a nanoindentation and microstructure surrounding the indent in Grain A, created from deflection data. A deflection image is useful here primarily as a visual aid. See Fig. 3 (*top*) for a height plot of this indent

tures observed. Slip may occur during plastic deformation in SMA materials, which produces slip lines on those planes. Slip occurs on close packed planes, and as such it is also a crystallographic property. In CuAlNi, (110) planes are close packed in austenite. Slip planes of (111) and (211) are also considered, as they are slip planes in other BCC structures. A review of the literature does not show any data on the slip planes in martensite. Fracture planes (566) and (765) have been observed in single crystal fracture experiments in CuAlNi and are also considered here [22].

A PERL program was used to rotate the vectors describing the various planes in which the deformations might occur. The intersection of the austenite–martensite interfaces, fracture planes, and slip planes with the crystallographic plane of observation were determined as a trace on the surface. The angles of these traces in the reference frame of the experimental results discussed above are summarized in Tables 1 and 2.

Discussion

As described above, the process zone under an indentation in an SMA is expected to involve elastic deformation, transformation, twin rearrangement, and plastic slip. The indentations studied here were conducted in the austenite phase, thus it is expected that the material beneath the indenter experiences elastic deformation, followed by stress induced martensite trans-

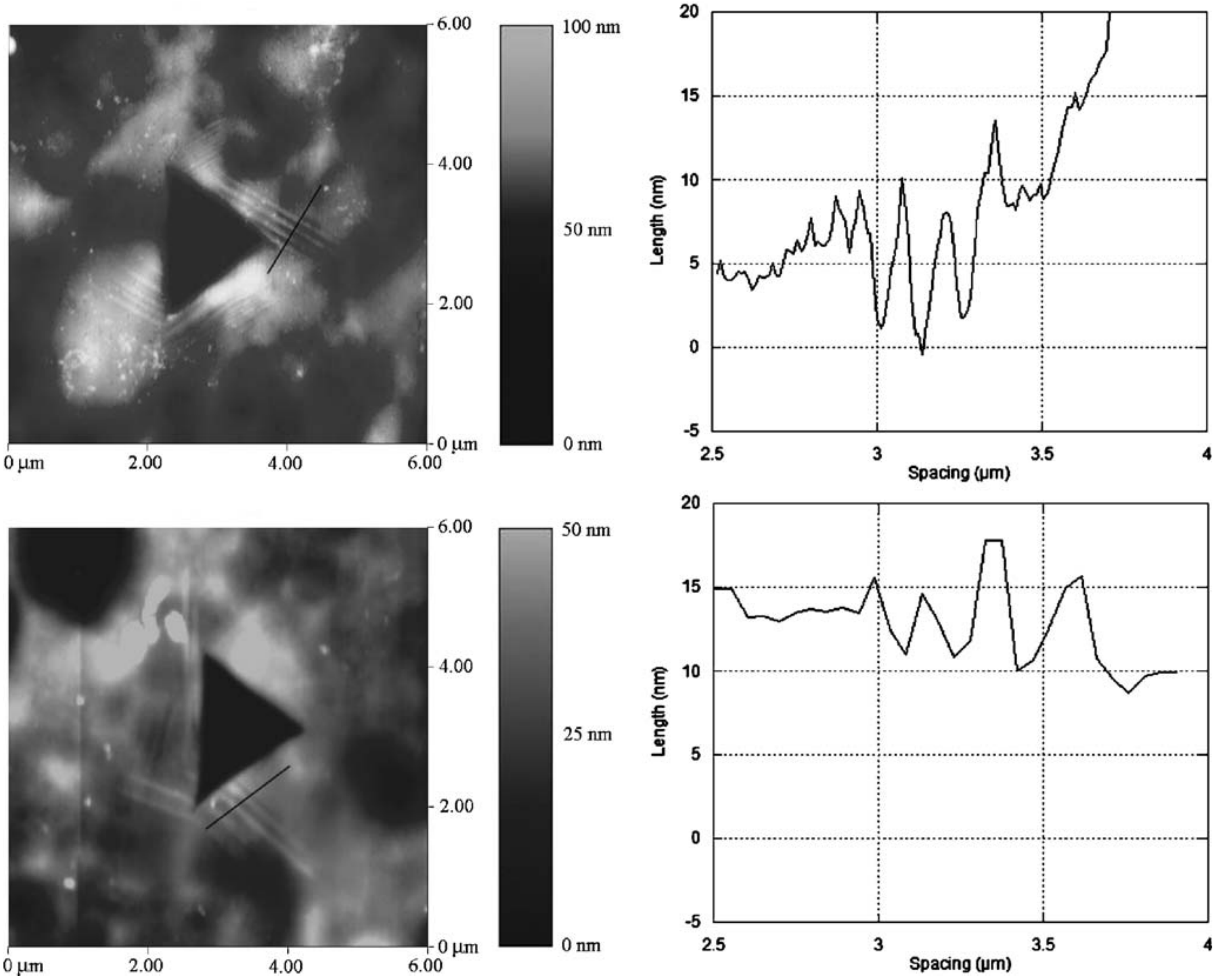

Fig. 3. Comparative view of nanoindentations in Grain B (*top*) and Grain A (*bottom*). Note the linear features emanating from the edges of the indentation. The height of these features is given in the cross-section plots, the range of which is denoted by the *black line* overlaid on each AFM image. Note that the scan for Grain A has one-quarter the resolution of Grain B, hence the loss in detail in the *bottom-right plot*

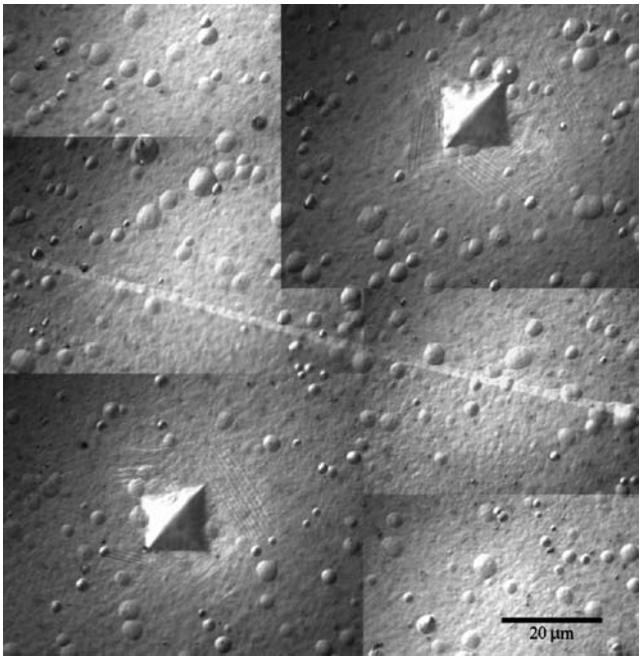

Fig. 4. DIC optical images of two microindentations, made with a Vickers tip are shown at room temperature. Grain A is located on the *lower-left* and Grain B on the *upper-right*. The grain boundary is visible as the *light colored line* across the center of the image. The indenter orientation is roughly the same while the resulting surface deformation differs. Refer to Fig. 1 for the crystallographic orientations of these grains

formation, elastic deformation in the martensite phase, and finally plastic deformation. The process zone, which is expected to be larger in extent than the indent contact area, should show evidence of some of these material states after the indentation is unloaded. Elastic deformation would recover with unloading of the indentation. Stress-induced martensitic transformation in the vicinity of the indentation would produce multiple variants of martensite, depending on the stress field caused by indentation. If no residual stress were present, unloading of the indentation would allow for reverse transformation to occur and material in the martensite phase would return to austenite. However, residual stress due to plastic deformation may lock in some of the martensite phase, which would allow austenite–martensite interfaces to remain in the material. Plastic deformation should be evident in the form of pile-up or slip lines. Fracture planes are the only other possible crystallographic phenomenon for this type of material. Thus, the linear features observed experimentally may be evidence of either martensite structures, slip bands, or fracture planes.

Proper surface preparation of the sample is a critical factor for making the nanoscale observations of interest in this study. Without the electropolishing step described above, nanoindentation results and subsequent AFM scans of the surface do not reveal the linear features of interest in this study. For example, when a CuAlNi sample was polished down to 1200 grit followed by colloidal silica and then indented, no obvious changes in surface morphology outside of pile-up in the immediate indent area can be observed. This is a result of the thin surface layer having been disturbed by the mechanical polishing process. In nanoscale work, this disturbed surface layer is appreciable and must be eliminated to obtain the results shown here. While the electropolishing process used here produced some pitting, there was suitable surface area in which to indent.

Fig. 5. DIC optical images of two microindentations made with different orientations of the Vickers indenter tip in Grain B are shown at room temperature

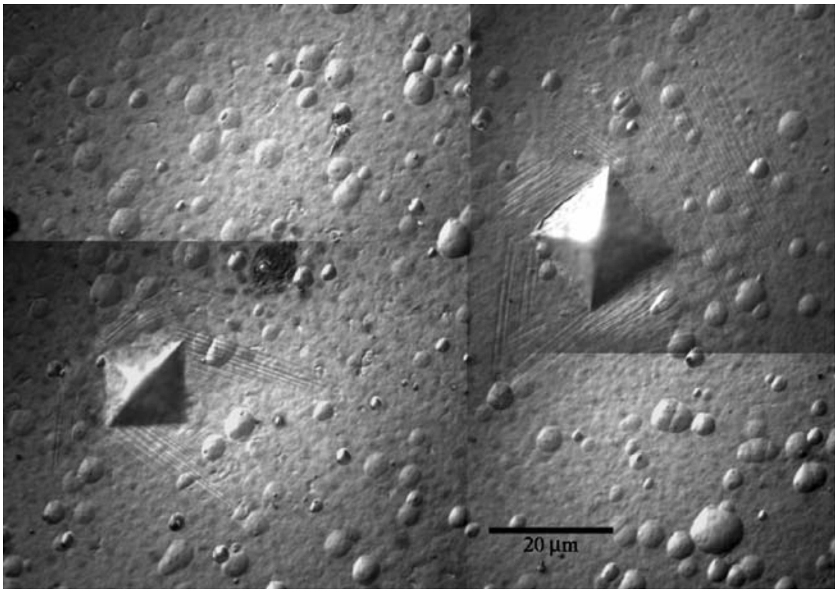

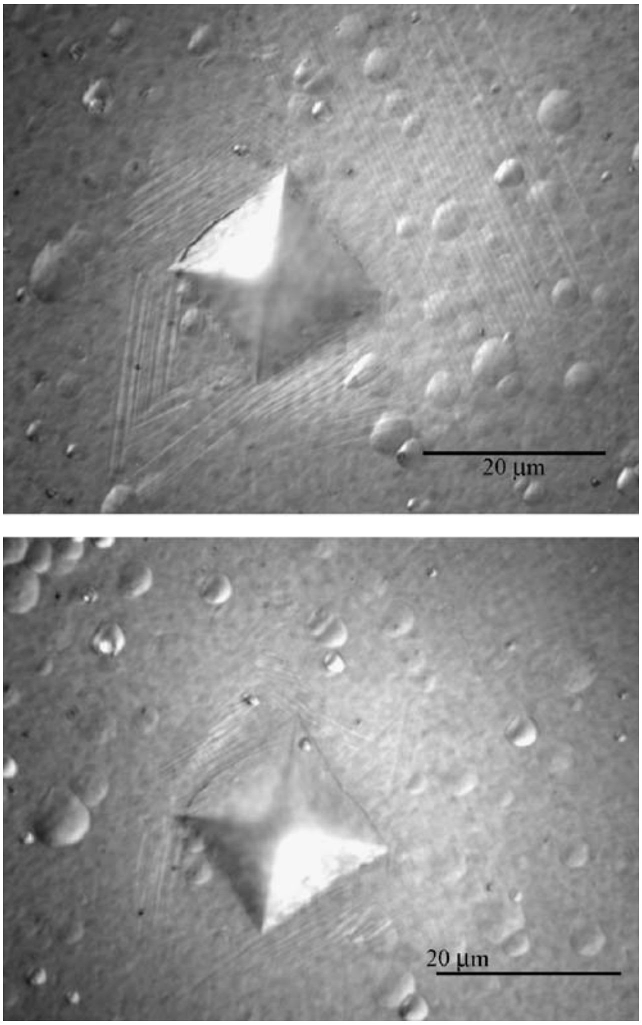

Fig. 6. DIC optical images of a microindentation in Grain B are shown at room temperature (*top*) and at 90°C (*bottom*). It is apparent that some surface features diminish or vanish as a consequence of heating. They are subsequently recovered upon cooling to room temperature

Unfortunately, other studies [6–8] do not use this type of surface preparation, which may be a reason that the same surface features reported here were not found after nanoindentation in these cited studies. Additionally, the changes in hardness at shallow depths reported [6] may not be as accurate compared to tests carried out on an electropolished sample. This polishing step is required to remove the disturbed surface layer created by mechanical polishing so that near-surface properties and crystallographic phenomena can be observed.

For the sample preparation used in this study, numerous linear features were observed after the indentation was unloaded. Because of the complex stress field produced by the indenter, the anisotropic nature of the crystal, and the differences in geometry between the Berkovich nanoindenter and the Vickers microindenter, the linear features observed around each type of indent differ in orientation. This is seen by comparing the nanoindentations of Fig. 3 with the microindentations of Fig. 4 for grains A and B (all images have the same reference frame). Moreover, there is interplay between the anisotropy of the material and the non-uniform stress state around the indenter which causes variation in the observations within a grain if the indenter tip is rotated, as seen in Fig. 5. For the microindent observations in NiTi, however, the surface features observed there were indifferent to indenter rotation [10].

In an effort to identify the origin of the linear features observed, crystallographic data was used to compare the linear features to the predicted austenite–martensite interfaces, slip planes and fracture planes. Tables 1 and 2 provide a summary of the possible angles observed for the crystallographic phenomena considered. Bold and italic notations highlight the correlation between calculated and observed angles of the linear features for nano- and microindentation, respectively. Of the 15 observed angles in two separate grains, matching angles (within the bounds of experimental error) are present for 14 predicted angles in the list of austenite–martensite interfaces. For the 110 slip planes, the most likely plastic deformation mode, only five matching angles are found. Thus, although some of the features could be either an austenite–martensite interface or a slip plane, the vast majority can be attributed to transformation processes. Other modes of deformation show substantially less agreement.

After these observations, thermal experiments were conducted while observing the microindentations.

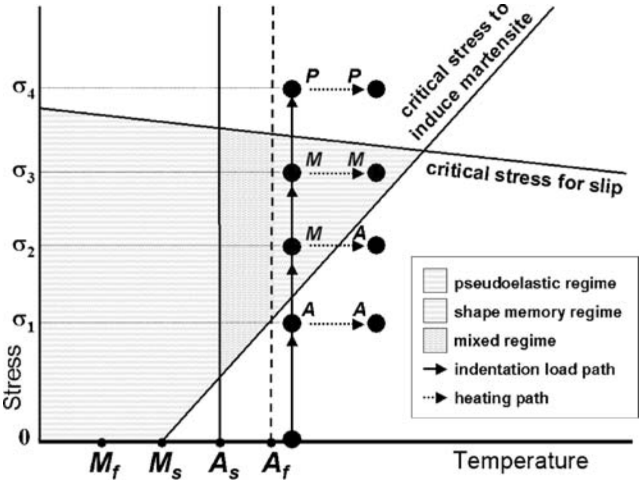

Fig. 7. Schematic phase diagram depicting indentation and subsequent heating. The transformation temperatures are shown as austenite start (A_s), austenite finish (A_f), martensite start (M_s), and martensite finish (M_f). Notations in the diagram are given for the austenite phase (A), the martensite phase (M), and plastically deformed material (P). (Diagram adapted from [23])

When heated, most of the linear features surrounding the indentation diminish in extent and many disappear entirely. For the indent shown in Fig. 6, features at −67.5°, +10°, +36.5°, and +80.5° are reduced in length or eliminated when heated to 90°C and reappear with cooling. Amongst the various microindentations studied in both grains, features at every angle except +65° were observed to diminish or vanish in at least one case of their occurrence, adding evidence to the supposition that these features are austenite–martensite interfaces.

The processes taking place in the indentation loading and subsequent heating cycle are explained schematically in Fig. 7. A range of stress states, σ_1 through σ_4, is depicted. These stresses correspond to the final stress states for material points at a range of distances from the far field (σ_1) to points near the indentation (σ_4). Alternatively, the vertical loading path could be interpreted as the path that a material point would traverse during the indentation process. Depending on the level of stress reached, the material point would remain in the austenite phase (A), transform to martensite (M) if the critical stress to induce martensite is exceeded, or plastically deform (P) if the critical stress to induce slip is exceeded. Heating causes material in the martensite phase (M) to transform to austenite (A) only if the temperature change is sufficient to move below the critical stress to induce martensite. The heating path depicted for σ_2 occurs for the linear features that disappear during the heating test. The features at +65° that remain upon heating may also be an austenite–martensite interface which follows the heating path depicted for σ_3. As Table 1 shows, there are no other possible explanations for this angle in the slip and fracture planes considered.

The only outstanding features remaining that do not appear to be austenite–martensite interfaces are the features at −30.5° for the nanoindentation in Grain B which occur on both sides of the indentation. Although they appear to be very similar to all of the other features observed, the angles do not correspond to an austenite–martensite interface. These features do correlate to angles possible for a (110) slip plane or a (765) fracture plane.

Conclusion

Nanoindentation and microindentation studies were conducted in large grains of CuAlNi tested in the austenite phase. Using carefully prepared CuAlNi samples, linear features can be observed surrounding the indentations after unloading. By comparison to possible deformation types it is concluded that these features are austenite–martensite interfaces which remain in the material after unloading as a consequence of the constraints of the deformation created by indentation. These stress-induced martensites are influenced by thermal changes and are observed to diminish with heating and reappear with cooling. These observations agree with the temperature dependence of the transformation stress in shape memory alloys. Plastic deformation is observed in the form of pile-up near the indentation.

Acknowledgments This research was made possible by grants from the Air Force Office of Scientific Research (AFOSR Award # FA9550-04-1-0109) and the National Science Foundation (NSF Award # CMS-0134385).

References

1. Oliver WC, Pharr GM (1992) An improved technique for determining hardness and elastic modulus using load and displacement sensing indentation experiments. J Mater Res 7:1564–1583, June.
2. Moyne S, Poilane C, Kitamura K, Miyazaki S, Delobelle P, Lexcellent C (1999) Analysis of the thermomechanical behavior of Ti–Ni shape memory alloy thin films by bulging and nanoindentation procedures. Mater Sci Eng A 275:727–732, December.
3. Shaw GA, Stone DS, Johnson AD, Ellis AB, Crone WC (2003) The shape memory effect in nanoindentation of nickel–titanium thin films. Appl Phys Lett 83(2):257–259.
4. Ni WY, Cheng Y-T, Grummon DS (2003) Microscopic superelastic behavior of a nickel–titanium alloy under complex loading conditions. Appl Phys Lett 82:2811–2813, April.
5. Ma X-G, Komvopoulos K (2003) Nanoscale pseudoelastic behavior of indented titanium–nickel films. Appl Phys Lett 83:3773–3775, November.
6. Liu C, Sun Q, Zhao Y, Yu T (2002) Depth dependence of nanohardness in a CuAlNi single crystal shape memory alloy. Int J of Nonlinear Sci & Numer Simul 3(3–4):535–538.
7. Liu C, Zhao Y, Sun Q, Yu T, Cao Z (2005) Characteristic of microscopic shape memory effect in a CuAlNi alloy by nanoindentation. J Mater Sci 40:1501–1504.
8. Liu C, Zhao Y, Yu T (2005) Measurement of microscopic deformation in a CuAlNi single crystal alloy by nanoindentation with a heating stage. Mater Des 26:465–468.
9. Ni W, Cheng Y, Grummon D (2002) Recovery of micro-indents in a nickel–titanium shape-memory alloy: a “self-healing” effect. Appl Phys Lett 80:3310.
10. Gall K, Juntunen K, Maier HJ, Sehitoglu H, Chumlyakov YI (2001) Instrumented micro-indentation of NiTi shape-memory alloys. Acta Mater 49:3205–3217, September.
11. Gall K, Dunn ML, Liu Y, Labossiere P, Sehitoglu H, Chumlyakov YI (2002) Micro and macro deformation of single crystal NiTi. J Eng Mater Technol 124:238–245.
12. Hane KF, Shield TW (1998) Symmetry and microstructure in martensites. Philos Mag A 78:1215–1252.

13. Hane KF, Shield TW (2000) Microstructure in the cubic to trigonal transition. Mater Sci Eng A291:147–159.
14. Hane KF, Shield TW (2000) Microstructure in a cubic to orthorhombic transition. J Elast 59:267–318.
15. Hane KF, Shield TW (1999) Microstructe in the cubic to monoclinic transition in titanium–nickel shape memory alloys. Acta Metall 47:2603–2617.
16. Hane KF (1998) Microstructures in thermoelastic martensites. PhD thesis, University of Minnesota.
17. Bhattacharya K (2003) Microstructure of martensite. Oxford University Press.
18. James RD, Hane KF (2000) Martensitic transformations and shape-memory materials. Acta Mater 48:197–222.
19. Vasko GM, Leo PH, Shield TW (2002) Prediction and observation of crack tip microstructure in shape memory CuAlNi single crystals. J Mech Phys Solids 50:1843–1867.
20. Shield TW (2005) “ctm-0.0.1” University of Minnesota, personal communication.
21. Shield TW (1995) Orientation dependence of the pseudoelastic behavior of single crystals of CuAlNi in tension. J Mech Phys Solids 43:869–895.
22. Loughran GM, Shield TW, Leo PH (2003) Fracture of shape memory CuAlNi single crystal. Int J Solids Struct 40:271–294.
23. Otsuka K, Wayman CM (1998) Mechanism of shape memory effect and superelasticity. In: Otsuka K, Wayman CM (eds) Shape Memory Materials. Cambridge University Press.